quaternary

MDPI

Article

Characterization of Heavy Minerals and Their Possible Sources in Quaternary Alluvial and Beach Sediments by an Integration of Microanalytical Data and Spectroscopy (FTIR, Raman and UV-Vis)

Adel A. Surour [1,2,*] and Amira M. El-Tohamy [3]

[1] Department of Geological Sciences, Faculty of Science, Galala University, New Galala City, Suez 43511, Egypt
[2] Geology Department, Faculty of Science, Cairo University, Giza 12613, Egypt
[3] Nuclear Materials Authority (NMA), Maadi P.O. Box 530, Cairo, Egypt; amira_eltohamy2011@yahoo.com
* Correspondence: adelsurour@hotmail.com or adel-surour@gu.edu.eg or adelsurour@cu.edu.eg

Abstract: Quaternary stream sediments and beach black sand in north-western Saudi Arabia (namely Wadi Thalbah, Wadi Haramil and Wadi Al Miyah) are characterized by the enrichment of heavy minerals. Concentrates of the heavy minerals in two size fractions (63–125 μm and 125–250 μm) are considered as potential sources of "strategic" accessory minerals. A combination of mineralogical, geochemical and spectroscopic data of opaque and non-opaque minerals is utilized as clues for provenance. ThO_2 (up to 17.46 wt%) is correlated with UO_2 (up to 7.18 wt%), indicating a possible uranothorite solid solution in zircon. Hafnoan zircon (3.6–5.75 wt% HfO_2) is a provenance indicator that indicates a granitic source, mostly highly fractionated granite. In addition, monazite characterizes the same felsic provenance with rare-earth element oxides (La, Ce, Nd and Sm amounting) up to 67.88 wt%. These contents of radionuclides and rare-earth elements assigned the investigated zircon and monazite as "strategic" minerals. In the bulk black sand, V_2O_5 (up to 0.36 wt%) and ZrO_2 (0.57 wt%) are correlated with percentages of magnetite and zircon. Skeletal or star-shaped Ti-magnetite is derived from the basaltic flows. Mn-bearing ilmenite, with up to 5.5 wt% MnO, is derived from the metasediments. The Fourier-transform infrared transmittance (FTIR) spectra indicate lattice vibrational modes of non-opaque silicate heavy minerals, e.g., amphiboles. In addition, the FTIR spectra show O-H vibrational stretching that is related to magnetite and Fe-oxyhydroxides, particularly in the magnetic fraction. Raman data indicate a Verwey transition in the spectrum of magnetite, which is partially replaced by possible ferrite/wüstite during the measurements. The Raman shifts at 223 cm^{-1} and 460 cm^{-1} indicate O-Ti-O symmetric stretching vibration and asymmetric stretching vibration of Fe-O bonding in the FeO_6 octahedra, respectively. The ultraviolet-visible-near infrared (UV-Vis-NIR) spectra confirm the dominance of ferric iron (Fe^{3+}) as well as some Si^{4+} transitions of magnetite (226 and 280 nm) in the opaque-rich fractions. Non-opaque heavy silicates such as hornblende and ferrohornblende are responsible for the 192 nm intensity band.

Keywords: zircon; monazite; Fe-Ti oxides; rare-earth elements (REEs); spectroscopic characterization; stream sediments; Saudi Arabia

Citation: Surour, A.A.; El-Tohamy, A.M. Characterization of Heavy Minerals and Their Possible Sources in Quaternary Alluvial and Beach Sediments by an Integration of Microanalytical Data and Spectroscopy (FTIR, Raman and UV-Vis). *Quaternary* **2024**, *7*, 46. https://doi.org/10.3390/quat7040046

Academic Editors: David J. Lowe and James B. Innes

Received: 30 June 2024
Revised: 2 October 2024
Accepted: 17 October 2024
Published: 22 October 2024

1. Introduction

In arid environments, such as those in the Arabian Peninsula and North Africa, the Neoproterozoic shield rocks known as "The Arabian-Nubian Shield (ANS)" are dissected by numerous dry streams or wadis. The study of heavy minerals in stream sediments in the wadis dissecting the ANS is of great importance because of its benefits in exploration programs for economic minerals such as gold, rare metals and radioactive materials [1–13]. In addition, the fingerprints of provenance or source areas in hinterlands are controlled by the geography, environment and alluvial sedimentation in aeolian environs [14–19].

In western Saudi Arabia, the coastal Red Sea sediments comprise consolidated siliciclastic sandstone (Miocene Raghama Formation) or loose beach sediments. Occasionally,

sand on the beach shows ripple marks, and is sometimes truncated by batches of black sand, gravel and oolitic carbonate fragments. Also, siliciclastic rocks extend to the Pliocene and are used to infer paleo-weathering, the paleo-climate and depositional environment [20,21]. Dry streams are filled with Quaternary alluvium, and in some instances in unconsolidated wadi terraces.

Spectroscopic methods are non-destructive and therefore they are widely utilized in earth sciences applications, such as mineralogy and others aiming to identify and characterize minerals as a function of their crystal chemistry and lattice ordering [22–26]. The applications of spectroscopy in mineralogy and economic geology are helpful for the study of heavy minerals, and accordingly, it provides precise characterization of minerals, in addition to details of the internal structure and helpful clues for provenance [22,27,28].

The present study does not aim to characterize the mineralogical composition of the investigated heavy fractions only but to give additional clues for provenance and economic potentiality. In recent years, international scholars have been interested in several mineral resources of the north-western territory of Saudi Arabia in the context of urban expansion, geotourism and the use of natural resources. Nowadays, international mining companies need detailed mineralogical and spectroscopic studies to integrate the exploration programs and the exploitation of heavy minerals in Saudi Arabia, particularly the so-called "strategic minerals". For this reason, the present work presents the first spectroscopic identification and characterization of potential economic minerals in the heavy concentrates along the Red Sea coast. The authors focus on the integration of the mineralogical, chemical and spectroscopic data of "strategic" minerals that would bear useful elements (e.g., U, Th and rare-earth elements, REEs). Also, it is aimed to benefit from the obtained analytical data for provenance characterization, and to connect them with Neoproterozoic rocks (Arabian Shield) and Phanerozoic volcanic fields (Saudi Harrats) in the hinterland.

2. Study Areas and Sampling

The Wadi Thalbah, Wadi Haramil and Wadi Al Miyah dissect Neoproterozoic rocks of the Madyan terrane of the ANS in north-western Saudi Arabia [29,30] (Figure 1). The Neoproterozoic rocks comprise a mafic–ultramafic association, island–arc plutonic and volcanic rocks, intra-mountainous molasse-type sediments, syn-collisional mafic and felsic plutonism, intra-plate felsic magmatism and finally Teriary to Neogene basalts of the Harrat Volcanic Fields (HVFs). In the study area, the oldest lithology is represented by layered/metamorphosed rocks as low-grade, greenschist facies metasediments and metavolcanics (Figure 1c). Intrusive arc-related rocks are dominated by gabbro, diorite and microdiorite. In contrast, the syn- and post-collisional stages are dominated by a fresh association of felsic intrusives known as the "younger granites", which include monzogranite, syenogranite and alkali feldspar granite. The "younger granites" are preceded by the so-called "Thalbah Group", which represents the molasses-type sediments that comprise conglomerate, mudstone and siltstone [29–32].

The investigated wadis are underlain by Quaternary and Neogene loose sediments in the form of wadi alluvium, wadi terraces and beach sediments. Stream sediments in the three wadis were previously explored for the potentiality of opaque minerals and gold. Moufti [9,31] focused on the recognition of Fe-Ti oxides and their primary and secondary intergrowths. In addition, ref. [31] paid attention to their abundance with respect to total opaque percentage in terms of the "figure index" and other sedimentological parameters such as sorting and skewness. Moufti [9] reported placer gold up to ~29 g/t in the finest silt fraction (<40 μm) extracted from the beach sands and wadi alluvium. In addition to the beach sediments, which comprise black sand batches on the narrow coastal plain, there is the Raghama Formation of Miocene clastic sedimentary rocks resting on the Neoproterozoic rocks non-conformably.

In the present study, loose sediments from five sites are investigated because they have a considerable heavy mineral concentrate. Amounts of heavy minerals obtained from the other sites are much smaller. As shown in Table 1, they comprise either black sand or wadi

alluvium in two size fractions within two ranges (63–125 µm and 125–250 µm, respectively). The heavy minerals percentage in the black sand samples lies in a narrow range (13.7 to 14.3%), whereas it is wider in the wadi alluvium (3.9 to 8.6%) (Table 1). The sample locations are shown in Figure 1b. Additionally, Table 1 provides additional information about the size and categorization of heavy minerals into opaque and non-opaque. Not all samples are categorized based on size because some of them are almost free of heavy mineral concentrate in the coarse fraction.

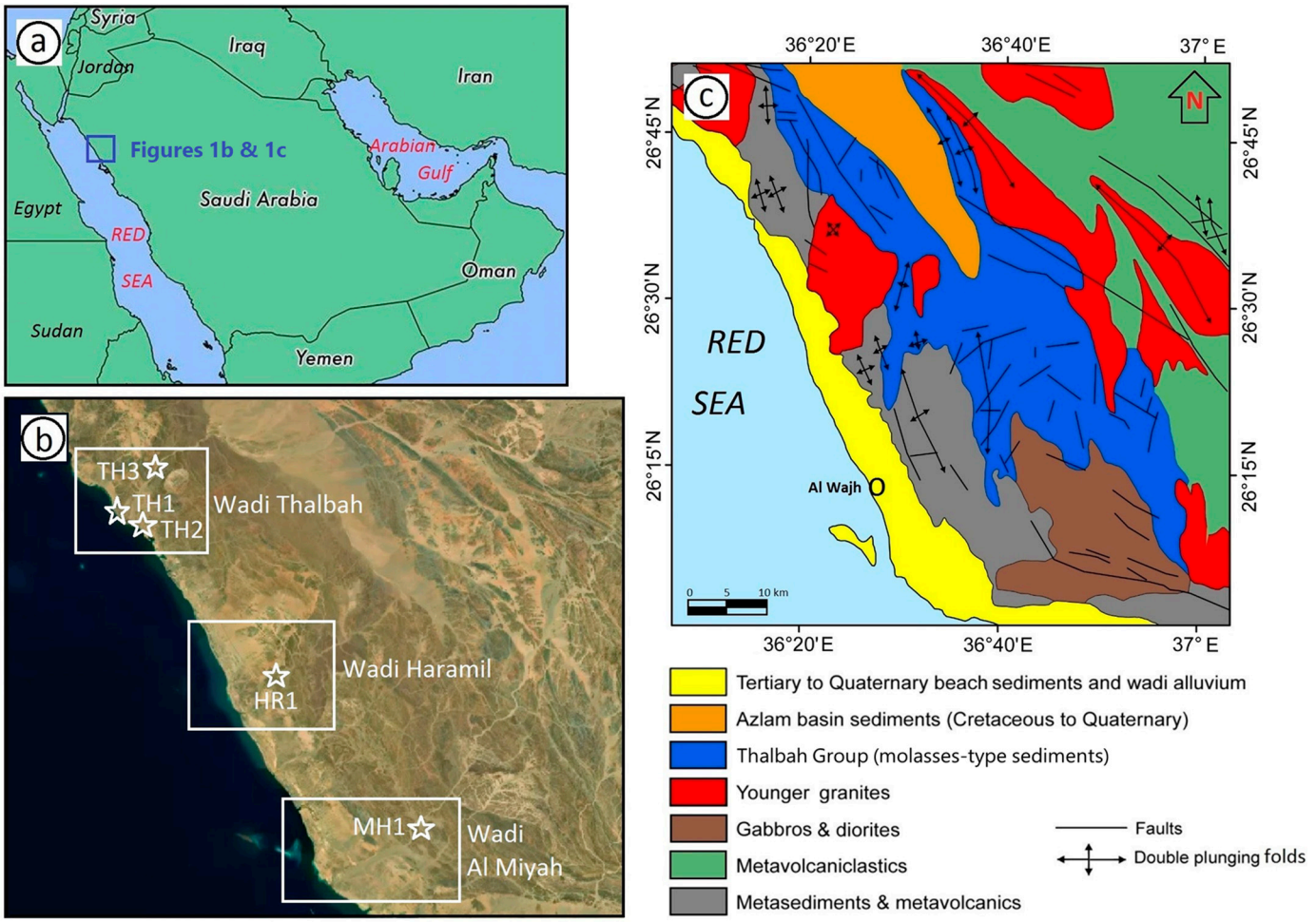

Figure 1. (**a**) Location map of the study area in north-western Saudi Arabia; (**b**) Sample locations in three investigated wadis shown on a Google-based satellite image; (**c**) Modified geological map of Al Wajh quadrangle based on lithological boundaries from [32] and updated nomenclature from [30].

Table 1. Sample location and characterization from three wadis *.

Site #	Location	Identification	Size Fraction	Heavy Minerals Content	
				Heavy Minerals %	Opaque %
TH1	26°39′55″ N 36°10′59″ E	Beach black sand	63–125 µm	14.3	53
TH1	26°39′55″ N 36°10′59″ E	Beach black sand	125–250 µm	14.3	55
TH2	26°39′55″ N 36°10′59″ E	Beach black sand	125–250 µm	13.7	57

Table 1. *Cont.*

Site #	Location	Identification	Size Fraction	Heavy Minerals Content	
				Heavy Minerals %	Opaque %
TH3	26°45′39″ N 36°18′48″ E	Wadi alluvium	63–125 μm	4.7	35
MH1	26°13′31″ N 36°40′59″ E	Wadi alluvium	63–125 μm	3.9	30
HR1	26°27′53″ N 36°28′14″ E	Wadi alluvium	125–250 μm	8.6	28

* Wadi Thalbah (TH) Wadi Al-Miyah (MH) Wadi Hramil (HR).

3. Materials and Methods

From each sample, heavy mineral concentrate was obtained by the heavy liquid separation method (bromoform, specific gravity = 2.81 g/cm^3). The heavy fractions were subjected to magnetic fractionation using a Frantz Isodynamic Magnetic Separator (Model LB 1) under the following conditions: transverse slope 5, longitudinal slope 20 and 0.2 amps step of current. Then, polished mounts were prepared for ore minerals identification and textures using a reflected light microscope. In addition, a scanning electron microscope model Prisma E SEM attached with an energy dispersive X-ray spectrometer (EDS) housed in the Nuclear Materials Authority of Egypt (NMA) was used for spot chemical analysis of minerals. Analytical conditions were 25–30 kV accelerating voltages, 1–3 nm beam resolution and 60–120 s counting time. The chemical composition of the eight studied samples was obtained by a portable XRF analyser at the Department of Geology, Cairo University, Egypt. An Oxford portable XRF analyser Model X-MET700 was used to analyse elements from K to U. The X-ray tube has a 40 kV Rh target, Si-PIN diode as a detector type, and the measurements were conducted at room temperature. Calibration was performed by a semi-quantitative method (FP) and quantitative traceable empirical calibrations. The used XRF analyser is accurate to less than ±0.01% for the measured elements. With respect to precision, the margin of error was determined based on 99.6% confidence for ±3δ (standard deviation). Generally, the range of precision lies between ±0.025% and ±0.072% whereas the margin of error ranges from ±0.0022% to ±0.0032%.

The FTIR analyses were conducted at the Micro-analytical Unit in the Faculty of Science, Cairo University, using a Jasco spectrophotometer Model 4100 working in the range 400–4000 cm^{-1} wave number with potassium bromide as a reference. This machine has a globar SiC source, a Ge-coated KBr beam splitter, and a liquid N_2-cooled HgCdTe detector. The FTIR spectra were collected under a nitrogen purge at 2 cm^{-1} pre-selected resolution at ~64 scans. The samples were pulverised, and discs were prepared by vacuum-pressing 2 mg of each sample with 198 mg of dried KBr. The KBr has a 100% transmittance of 100% in the range of Raman shifts 4000–400 cm^{-1}. The Raman analyses were conducted using a German-made confocal Raman microscope Model WItec 300R housed at the Raman Laboratory in the National Research Centre of Egypt in Dokki. The micro-Raman system worked at 473/532/633 nm laser excitation, z-focus, and a software-controlled x-y sample stage for line scanning and mapping. The obtained spectra were as high as 785 nm excitation wavelength. The IR beam's incidence angle was 45°, and 100 scans were collected at a resolution of 4 cm^{-1} and a mirror velocity of 0.6329 cm/s. The spectra were collected within the range of a 4000–400 cm^{-1} wave number. The spectra were co-added in order to improve the signal-to-noise ratio. The UV-Vis-NIR spectra were obtained using a Jasco double-beam spectrometer Model V770 housed at the National Research Centre of Egypt in Dokki. The samples were analysed in the 190–2500 nm spectral range, with a spectral bandwidth of 5 nm for the UV-Vis region and 20 nm for the NIR region. The data interval was 2 nm, and the scan speed was 1000 nm/min with 0.24 s response for both UV-Vis and NIR. For the studied heavy concentrates, polarised spectra using a diffraction grating polarizer were recorded.

4. Microscopic Investigation

4.1. Beach Black Sand

Opaque minerals (55–57% out of the total heavy minerals, Table 1) in the fine black sand (125–250 µm) from the mouth of Wadi Thalbah on the beach are represented mostly by homogeneous and intergrown Fe-Ti oxides (Figure 2a,b, respectively). Based on the investigation by the reflected light microscope, the ratio of homogeneous ilmenite to homogeneous magnetite amounts was 3:1, and some of the magnetite has a skeletal or star-shaped habit (Figure 2a). The investigated samples contain a variety of primary Fe-Ti intergrowths, mostly ilmenite-magnetite (ilmenomagnetite) and hematite-ilmenite (hemo-ilmenite) exsolution textures. Types of the primary ilmenite-magnetite intergrowth are sandwich, banded, composite, fine network and coarse-trellis exsolution textures. In this case, the host magnetite is relatively fresher than the exsolved ilmenite lamellae, which are highly replaced by either titanite or sub-graphic rutile-hematite (i.e., secondary intergrowth). Titanite is not always an intergrown phase, and it sometimes form a "rind" or a continuous reaction rim of homogeneous ilmenite (Figure 2c). In a few instances, homogeneous ilmenite is euhedral and fresh (Figure 2d).

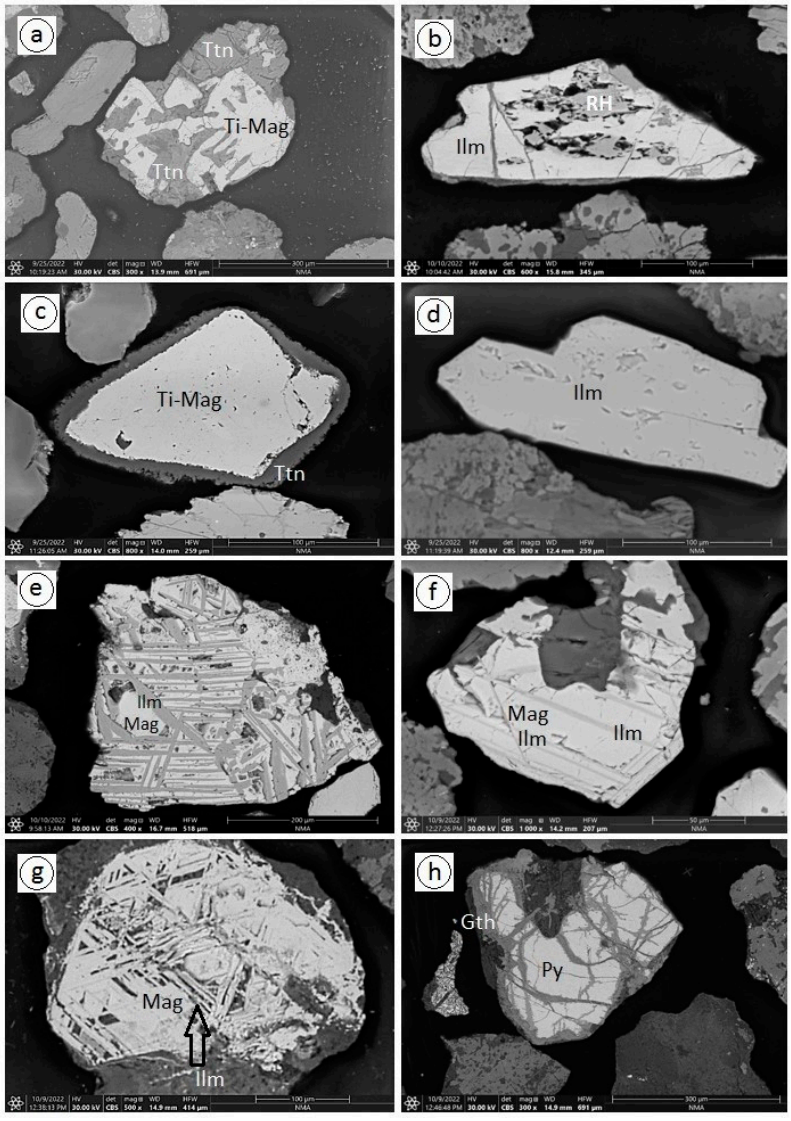

Figure 2. Opaque minerals in the heavy concentrates. (**a**) Skeletal Ti-bearing magnetite (Ti-Mag) and titanite (Ttn), coarse black sand, Wadi Thalbah; (**b**) Homogeneous ilmenite (Ilm) partly replaced by

sub-graphic intergrowth of rutile and hematite (RH), coarse black sand, Wadi Thalbah; (**c**) Homogeneous ilmenite (Ilm) with continuous titanite reaction rim (Tnt), fine black sand, Wadi Thalbah. (**d**) Freshness and euhedrality of homogeneous ilmenite (Ilm), fine black sand, Wadi Thalbah; (**e**) Coarse-trellis ilmenite (Ilm)-magnetite (Mag) intergrowth, fine wadi alluvium, Wadi Al Miyah. (**f**) Banded ilmenite (Ilm)-magnetite (Mag) intergrowth, fine wadi alluvium, Wadi Al Miyah; (**g**) Fine exsolved ilmenite (Ilm) confined to the (111) octahedral planes in host magnetite (Mag) forming fine network intergrowth, coarse wadi alluvium, Wadi Haramil; (**h**) Alteration of pyrite (Py) to goethite (Gth) along fractures and peripheries, coarse wadi alluvium, Wadi Haramil.

Sulphides do not exceed 2–3 % of the total opaques, and are represented by pyrite, which occurs in two different forms. The first form of pyrite is fine sub-rounded inclusions in homogeneous Fe-Ti oxides, whereas the second form of pyrite occurs as coarse independent grains that are extensively replaced by colloform goethite and Fe-oxyhydroxides. In the very fine black sand (63–125 μm), opaque minerals amount to 53% and the content of their Fe-Ti oxides is identical to the coarser fraction with the exception of less abundant hemo-ilmenite. The fine sand lacks any sulphide mineral in addition to noticeable higher degree of magnetite oxidation to martite.

4.2. Wadi Alluvium

As shown in Table 1, the lowest number of opaque minerals was in the coarse-sized concentrate (125–250 μm) from Wadi Haramil (28%). On the other hand, the lowest number of opaque minerals was observed in the 63–125 μm finer fraction from Wadi Al Miyah (30%) and Wadi Thalbah (35%). In the coarse-sized concentrate from Wadi Haramil, opaque minerals are represented by either homogeneous or ilmenite–magnetite intergrowths that are commonly partially replaced by titanite and hematite. Some primary ilmenite–magnetite exsolutions are present, e.g., coarse-trellis, banded and fine network (Figure 2e–g) whereas hemo-ilmenite is lacking. In a few instances, possible tiny gold is seen in the secondary titanite forming at the expense of Fe-Ti oxides, mostly Ti-bearing magnetite.

In the fine-sized heavy concentrates from the main courses of Wadi Thalbah and Wadi Al Miyah, opaque minerals are represented by Fe-Ti oxides, Fe-oxyhydroxides and sulphides amounting to 85%, 13% and 2%, respectively, of the total opaque percentage. The Fe-Ti oxides are represented by either homogeneous ilmenite and magnetite or a variety of their primary and secondary intergrowths. They show variable degrees of alteration. Homogeneous ilmenite and homogeneous magnetite occur in nearly equal amounts, 44% and 41% of the total opaque percentage, respectively. In particular, the fine-sized heavy concentrate from Wadi Al Miyah is characterised by considerable amounts of recrystallised homogeneous ilmenite with amoeba-like inclusions of silicates. Homogeneous ilmenite contains nucleus-like inclusions of pyrite. In addition, pyrite alters to goethite and Fe-oxyhdroxides along the fractures and peripheries (Figure 2h).

5. Chemical Analysis

Table 2 includes six representative analyses of heavy fractions, three from black sand and three from alluvium. This table distinguishes major oxides (94.6 to 96.9 wt%) from minor oxides (0.4 to 1.4 wt%). Among the major oxides, the most abundant are SiO_2, TiO_2, Al_2O_3, $Fe_2O_3{}^t$ and CaO. The range of silica in the black sand is wide (23.8 to 34.4 wt%) whereas it is narrow in the wadi alluvium (36.3 to 38.8 wt%). As a function of its content of Ti-bearing minerals (e.g., ilmenite, Ti-magnetite and titanite), TiO_2 content in the black sand is almost triple the content in the wadi alluvium (up to 4.3 wt% and up to 13.7 wt%, respectively). There is a relative enrichment of $Fe_2O_3{}^t$ in the black sand compared with the wadi alluvium (28.2 to 33.74 wt% and 31 to 40.3 wt%, respectively). Analyses in Table 2 show that there is little difference in the CaO content in the black sand and wadi alluvium (8 to 12.1 wt% and 6.6 to 9.4 wt%, respectively). On the other hand, the Al_2O_3 content varies distinctly from that of the black sand (6.7 to 8 wt%) to that of the wadi alluvium (9.9 to 13.3 wt%) taking into consideration that the latter is silicate-rich whereas the former is

silicate-poor. Among the minor oxides, contents of V_2O_5 and ZrO_2 are very characteristic in black sand (up to 0.4 wt% and up to 0.6 wt%, respectively). In contrast, V_2O_5 is under the limit of detection whereas the ZrO_2 content never exceeds 0.3 wt%.

Some spot EDS-EDX analyses of minerals from the heavy fractions in the five stations are provided in Table 3. This table distinguishes non-opaque minerals (monazite and zircon) from opaque minerals (two varieties of ilmenite and two varieties of magnetite). The monazite s by default has a large content of rare-earth element oxides (up to 67.9 wt%). In zircon, ThO_2 and UO_2 amount to 16.1–17.5 wt% and 5.83–7.18 wt%, respectively, due to an appreciable substitution of Zr^{4+} by Th^{4+} and U^{4+}.

Table 2. XRF bulk composition of major and minor oxides.

Sample No. *	TH1	TH2	TH5	TH4	MH6	RH3
Major oxides (wt%)						
SiO_2	28	34.4	23.8	36.3	38.8	36.7
TiO_2	10.5	9.4	13.7	4.3	4	4.3
Al_2O_3	7.7	8	6.7	9.9	13.3	12.1
$Fe_2O_3{}^t$ **	36	31	40.2	33.1	28.2	33.7
CaO	10.7	12.1	8	9.4	9.1	6.6
MnO	0.8	0.7	0.99	0.7	0.7	0.5
K_2O	0.6	0.7	0.5	1	1	1.1
P_2O_5	0.9	0.6	0.9	1.1	1	0.8
Total ***	95.2	96.9	94.7	95.1	96.1	95.8
Minor oxides (wt%)						
RbO	0.02	0.01	n.d.	0.01	0.03	0.01
BaO	n.d.	n.d.	0.31	n.d.	n.d.	n.d.
SrO	0.18	0.22	0.13	0.14	0.13	0.11
Cr_2O_3	0.18	n.d.	n.d.	n.d.	n.d.	n.d.
CoO	n.d.	n.d.	n.d.	n.d.	n.d.	0.4
NiO	0.01	0.01	0.01	0.01	0.01	0.01
V_2O_5	0.36	n.d.	0.34	n.d.	n.d.	n.d.
ZrO_2	0.14	0.09	0.57	0.26	0.08	0.09
Nb_2O_5	0.04	0.03	0.04	0.03	0.01	0.01
ZnO	0.05	0.04	0.04	0.05	0.06	0.02
MoO_3	0.02	n.d.	n.d.	n.d.	0.02	n.d.
CdO	0.01	0.01	n.d.	n.d.	n.d.	n.d.
HgO	0.01	n.d.	n.d.	0.01	0.01	0.01
Total	1.02	0.41	1.44	0.51	0.35	0.66

* TH1: Beach black sand, Wadi Thalbah (63–125 μm); TH2 and TH5: Beach black sand, Wadi Thalbah (125–250 μm); TH4: Wadi alluvium, Wadi Thalbah (63–125 μm); MH6: Wadi alluvium, Wadi Al-Miyah (63–125 μm); HR3: Wadi alluvium, Wadi Haramil (125–250 μm); ** Total iron as ferric and n.d.: not detected; *** Loss on ignition was not determined.

Table 3. Semi-quantitative SEM-EDX analyses of heavy minerals (non-opaque and opaque).

Non-Opaque Minerals														
Monazite						Zircon								
P_2O_5	18.9	16	22.7	24.6	23	SiO_2	42.1	39.5	37.5	35.1	32.7	44.9	28.8	26
Al_2O_3	5.4	8.6	n.d. *	9.2	n.d.	ZrO_2	52.6	48.4	57.1	61.2	59	46.9	33.7	38.5
SiO_2	7	11.7	3.7	5.6	2.2	HfO_2	5.6	3.6	5.4	3.7	5.5	3.8	7.7	3.8
ThO_2	10.5	6.3	3.6	6	4.1	ThO_2	n.d.	n.d.	n.d.	n.d.	n.d.	n.d.	17.5	16.1
UO_2	2.3	1.3	1.2	3.1	1.1	UO_2	n.d.	n.d.	n.d.	n.d.	n.d.	n.d.	5.8	7.2
CaO	2.4	1.1	4.4	3.8	1.6	FeO **	n.d.	5.4	n.d.	n.d.	2.8	4.5	2.4	5
FeO **	1.6	3.8	3.3	2.7	n.d.	CaO	n.d.	3.2	n.d.	n.d.	n.d.	n.d.	4.1	3.5
REE Oxides	52	51.4	61.1	45.3	67.9									

Table 3. *Cont.*

Opaque Minerals											
Mn-free ilmenite								Mn-bearing ilmenite			
TiO_2	41.9	40.2	48.6	39.9	48.2	46.2	45.8	TiO_2	43	367	45.5
FeO **	58.1	59.8	51.4	37.3	41.2	43.2	45.2	FeO **	51.5	58.5	50.6
SiO_2	n.d.	n.d.	n.d.	12.1	6.8	6	5.1	MnO	5.5	4.5	3.9
CaO	n.d.	n.d.	n.d.	10.7	3.8	4.6	3.8				
Ti-bearing magnetite											
$FeO + Fe_2O_3$		95.8	93.1	94.5							
TiO_2		4.2	6.9	5.5							

* n.d.: not detected ** FeO: Total iron was ferrous in all except for magnetite (ferrous and ferric).

6. Discussion

6.1. Significance of Whole-Fraction Chemistry

Data given in Tables 1–3 summarize the characteristics, XRF composition of the heavy concentrates (whole-fraction: magnetic and non-magnetic) and the EDS-EDX microanalyses of heavy minerals. We constructed six binary diagrams (Figure 3) based on data from Table 2 in order to show the behaviour of the most abundant major and minor oxides in the bulk concentrate or the whole-fraction. From these binary plots, it is evident that the behaviour of oxides in the black sand and wadi alluvium follows the same trends, and therefore they are plotted together. These plots suggest that the most abundant oxides are the major ones, namely SiO_2, CaO, Al_2O_3, $Fe_2O_3{}^t$, TiO_2 and P_2O_5. Among minor oxides, SrO_2 only can correlate. Low content of V_2O_5 in the black sand (up to 0.36 wt% only) indicates a very minor substitution of V^{5+} in the magnetite structure for Fe^{2+} and Fe^{3+}, which is common in natural magnetites, especially in those derived from mafic igneous rocks [33–37]. In Saudi Arabia, a source of V-bearing magnetite is the layered mafic-ultramafic intrusions. They are layered intrusions formed in either arc or post-collisional settings [38–40], which are similar to intrusions hosting V-Fe-Ti ores in other parts in the Arabian-Nubian-Shield (e.g., [41,42]).

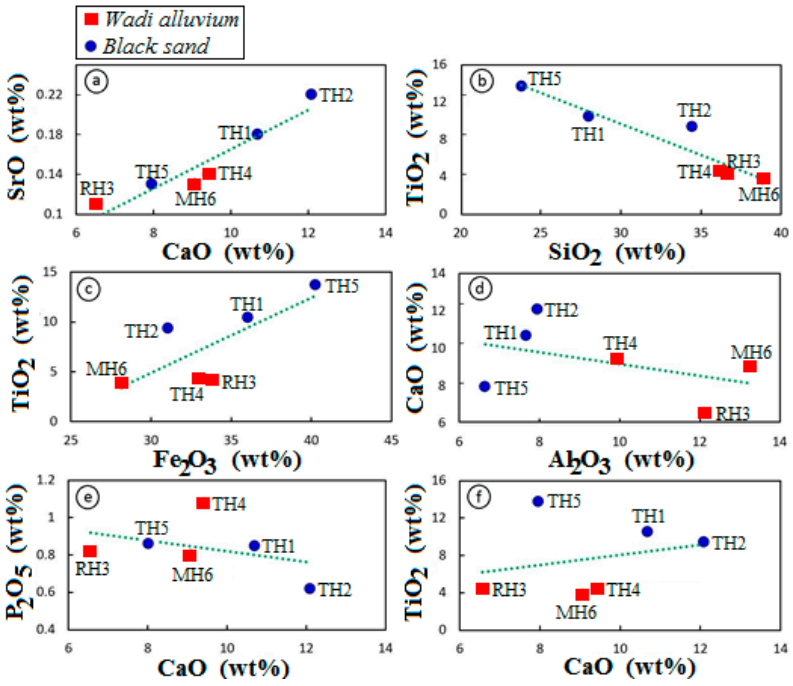

Figure 3. Binary relationships of some major oxides in the heavy concentrates whole-fractions (magnetic and non-magnetic).

Figure 3a shows that the best proportional relationship exists between CaO and SrO (R^2 = 0.8973). In the investigated heavy concentrates, both elements are encountered in the structure of non-opaques, mostly Ca-bearing amphibole. In nature, as well as experimentally, Ca^{2+} can be replaced totally in the M2- and M4-sites by Sr^{2+} [43]. On the other hand, a good regression trend (R^2 = 0.8856) is obtained from a reverse relationship between SiO_2 and TiO_2 (Figure 3b). Normally, TiO_2 decreases when Ti-bearing opaque minerals are minimal while primary silicate minerals dominate. Some secondary silicate, e.g., titanite replacing Ti-magnetite and ilmenite, can bear some Ti^{4+} as well. The relationship between $Fe_2O_3{}^t$ and TiO_2 is proportional (R^2 = 0.5743) (Figure 3c). In fact, this is common in stream sediments that are characterized by magnetite- and ilmenite-rich concentrates, which is the case of the investigated black sand. In northwestern Saudi Arabia, iron and titanium are positively correlated either in Fe-Ti-P ore or its host gabbros [44]. Contents of Al_2O_3 vs. CaO, CaO vs. P_2O_5 and CaO vs. TiO_2 are poorly correlated (Figure 3d–f) with low regressions (0.1807, 0.1442 and 0.0658, respectively). The relationship between CaO and P_2O_5 suggests a minimal influence of accessory apatite, which is neither seen microscopically nor by EDX microanalysis. Although the relationship between CaO and TiO_2 is weak, it is an indicator of the alteration degree of Ti-bearing opaque minerals into titanite [45,46].

6.2. Mineral Chemistry as an Indicator of Source Rocks

The microanalytical data presented in Table 3 include spot analyses of non-opaque minerals (monazite and zircon) and opaque minerals (Fe-Ti oxides) from the investigated samples from NW Saudi Arabia. The chemistries of heavy minerals in stream sediments and economic placer deposits such as black sand are very helpful for identifying the source rocks in the hinterlands, i.e., the provenance. In the Arabian-Nubian Shield of Egypt and Saudi Arabia, some studies connected mineral chemistry with the source rock of stream sediments (e.g., [2–5,9–11,13,14,31,37,47–50]). In the present study, we pay special attention to accessory or "strategic" non-opaque minerals, mostly zircon and monazite. BSE images and spectral analyses of these minerals are given in Figures 4 and 5 representing black sand and wadi alluvium, respectively).

In the heavy concentrates, compositions of zircon indicate it is U- and Th-free (Table 3). According to [2], zircon in the stream sediments derived from granitic rocks of the Neoproterozoic shield rocks are either U-free or U-bearing. However, analyses of zircon from the current Saudi examples are Hf-bearing with HfO_2 in the range 3.6–5.75 wt% indicating a mixed source from I-type and highly fractionated granites, i.e., calc-alkaline and alkaline [51,52]. Owing to its minute size and its being hosted by magnetite, the analysed zircon has some Fe impurities (2.77–5.35 wt% FeO^t). Also, Table 3 provides two analyses of an unidentified Zr-silicate phase, which is not a typical zircon and it contains large amounts of UO_2 (5.83–7.18 wt%) and ThO_2 (16.8–17.46 wt%). A possible mixture of zircon and uranothorite should therefore not be discarded. Analyses of monazite (Table 3) indicate some impurities of Si, Al, Ca and Fe. Such impurities are attributed to the tiny size of the monazite and therefore impurities are detected from the host minerals. P_2O_5 amounts to 23.04 wt% but sometimes SiO_2 from the background silicates dilutes P_2O_5 to become as low as 15.99 wt% when silica reaches its maximum content (11.65 wt%). A felsic source is assigned to the source of the monazite, particularly highly fractionated granites, which is also supported by the presence of an appreciable UO_2 and ThO_2 content (up to 3.12 wt% and 10.48 wt%, respectively). In a previous study, monazite from Wadi Thalbah stream sediments monazite was not uraniferous but contained 8.13 wt% ThO_2 [31]. Other support for a highly fractionated granite source is the rare-earth elements content (up to 67.88 wt% oxides of La, Ce, Nd, and Sm). This is also accepted by some authors such as [3,50]. Monazite in northern Saudi Arabia is multi-sourced from syenogranite, monzogranite, alkali feldspar granite and alkali amphibole granite. Therefore, the chemistry of monazite is variable and depends on the content of U and Th in the felsic melt, fractionation and additional magmatic processes for granites developed in an almost 100 Ma time span

(630–530 Ma ago) coinciding with the transition from the very late Neoproterozoic to the Cambrian [29–32].

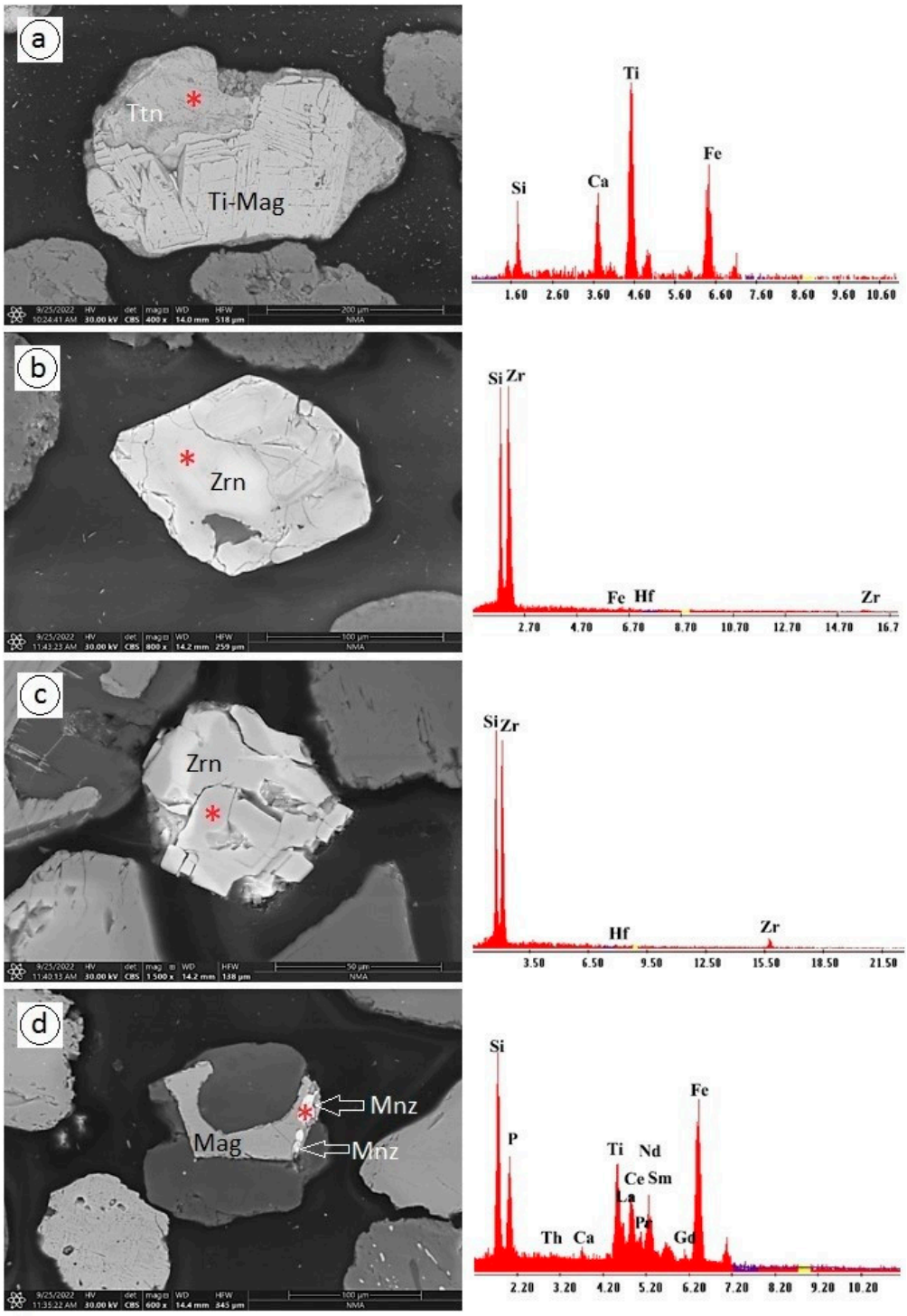

Figure 4. BSE images and spectral analyses of non-opaque accessory minerals from black sand from Wadi Thalbah. (**a**) Secondary titanite (Tnt) forms at the expense of Ti-bearing magnetite (Ti-Mag); (**b**) Fractured euhedral zircon (Zrn); (**c**) Fractured anhedral zircon (Zrn); (**d**) Interlocked silicate (grey) and magnetite (Mag) with minute inclusions of monazite (Mnz). A red Astrix is added to indicate exact position of analysis.

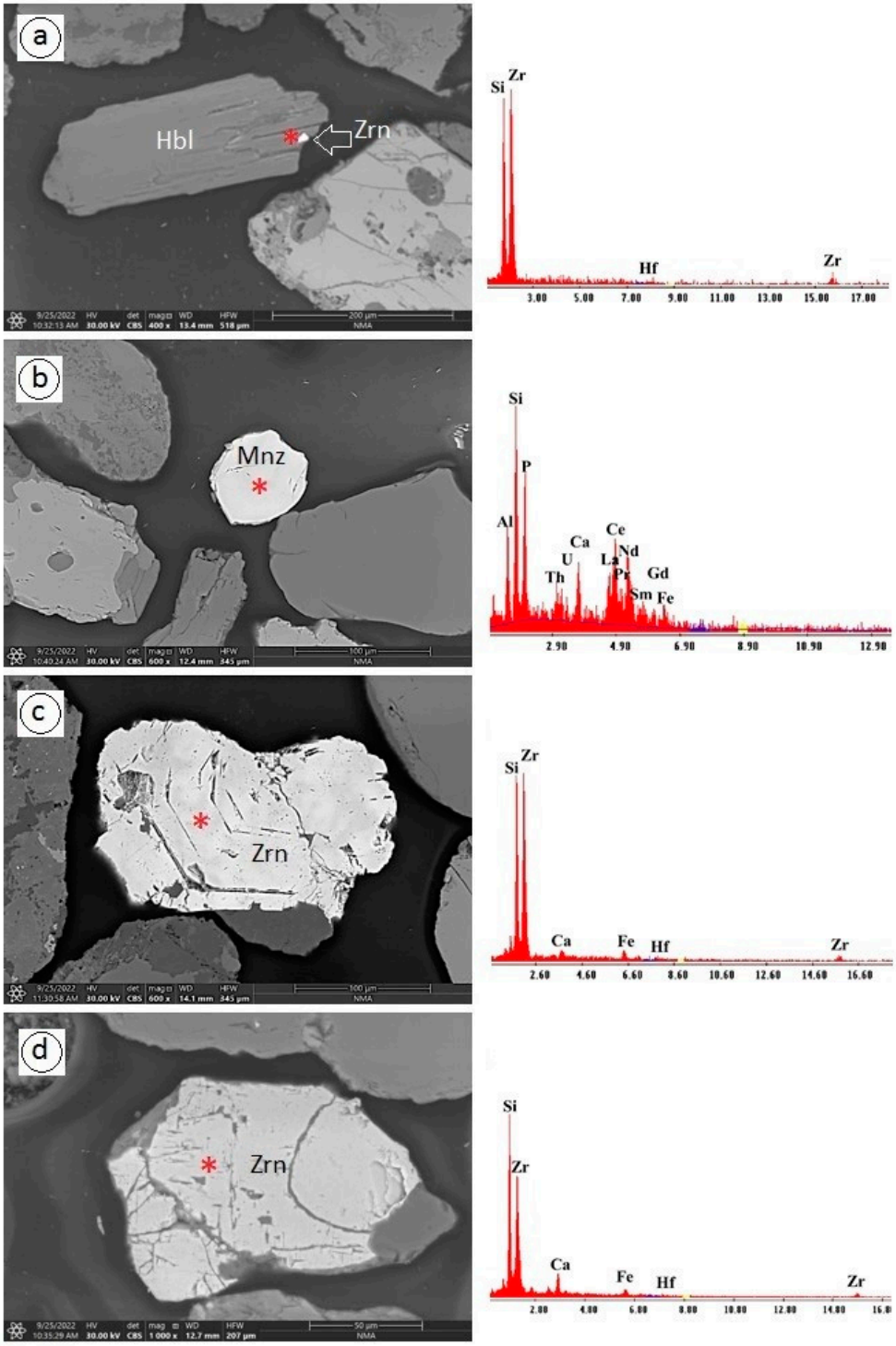

Figure 5. BSE images and spectral analyses of non-opaque accessory minerals from the wadi alluvium. (**a**) Extremely fine zircon (Zrn) at the peripheral zone of coarse hornblende (Hbl), fine fraction, Wadi Thalbah; (**b**) Subhedral U- and Th-bearing monazite (Mnz), fine fraction, Wadi Thalbah; (**c**) Anhedral zoned zircon (Zrn), fine fraction Wadi Al Miyah; (**d**) Fractured anhedral zircon (Zrn), coarse fraction, Wadi Al Miyah. A red Astrix is added to indicate exact position of analysis.

In a single drainage basin, the chemistry of detrital ilmenite is used as a helpful tool for the assignment of different provenances [53]. The analysed opaque minerals are classified as two ilmenite varieties (Mn-free and Mn-bearing), in addition to one magnetite variety (Ti-bearing) (Table 3). The Mn-free ilmenite itself can be distinguished into two sub-varieties; namely homogeneous (Si- and Ca-free) and exsolved lamellae with considerable

amounts of SiO_2 and CaO totalling 12.08 wt% and 10.74, respectively. Based on careful ore microscopic investigation and the microanalysis of exsolved ilmenite, Si and Ca are attributed to partial alteration to titanite [3,11,35,54–56]. Owing to a lack of Mg in the analysed Mn-free ilmenite, it is believed to have originated from a felsic igneous rock rather than a mafic rock [57,58]. On the other hand, Mn-bearing ilmenite contains 4.51–5.5 wt% MnO and can be considered as manganoan ilmenite. Petrological studies confirm geikielite ($MgTiO_3$) or pyrophanite ($MnTiO_3$) in solid solutions with ilmenite ($FeTiO_3$) favourably in a metamorphic condition [57,59,60]. Therefore, we can assign a metamorphic origin for our Mn-bearing ilmenite and it is possibly derived from mafic metasediments. TiO_2 in Ti-bearing magnetite reaches up to 6.88 wt% (Table 3). In north-western Saudi Arabia, the most probable source of Ti-bearing magnetite is the Phanerozoic Harrat Volcanic Fields, and to a lesser extent the arc and post-collisional fresh gabbros [39,61].

6.3. Spectroscopic Characterization

Combined FTIR, Raman and UV-Vis-NIR spectral analyses of the investigated heavy concentrates are given in Figures 6 and 7. It can be seen that the bands are sharp and show strong intensities, which indicate a high a degree of crystallinity and a lack of amorphous or non-crystalline phases. For decades, infrared spectroscopy proved its usefulness for accurate identification and characterization of inorganic substances with an ordered crystalline structure such as minerals [62]. Also, the era of spectroscopy in mineralogical studies witnessed great achievements, especially in applied fields such as gemological and archaeological research (e.g., [63,64]). In this respect, infrared spectroscopic characterization of loose sediments with considerable contents of heavy minerals, and from beaches as well as in streams and dry valleys/wadis [65], is a useful technique. Raman spectroscopy is very helpful for discriminating Fe-Ti oxides either in terrestrial or lunar samples using different excitation wavelengths (e.g., [27,66]).

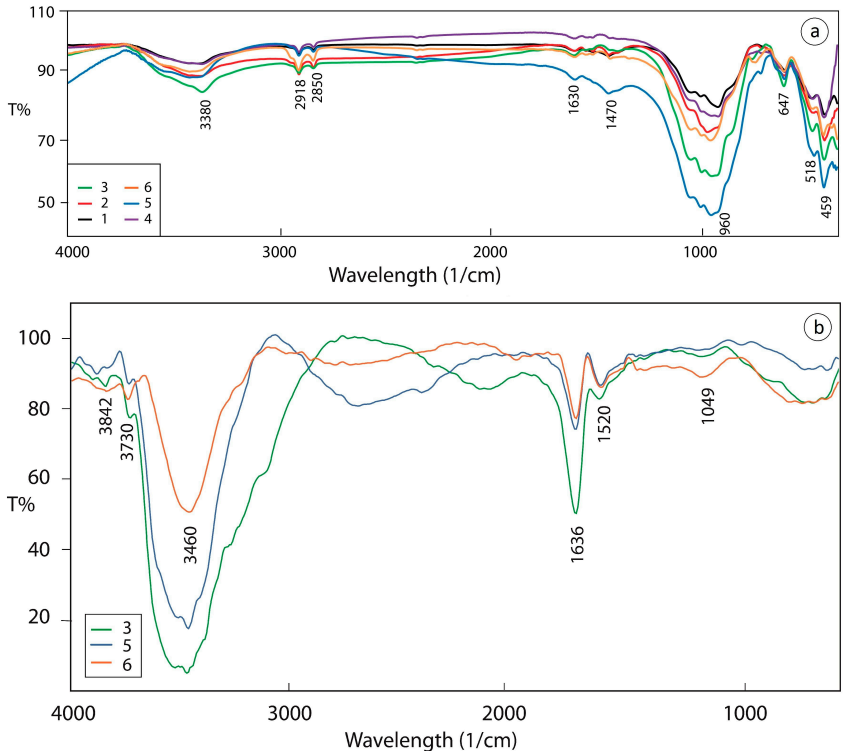

Figure 6. FTIR spectra of the heavy concentrates. (**a**) Bulk/whole-fraction (magnetic and non-magnetic); (**b**) Three representative magnetic fractions. (1) Fine black sand, Wadi Thalbah, (2) Coarse black sand, Wadi Thalbah, (3) Fine wadi alluvium, Wadi Al Miyah, (4) Fine wadi alluvium, Wadi Thalbah, (5) Coarse black sand, Wadi Thalbah, and (6) Coarse wadi alluvium, Wadi Haramil.

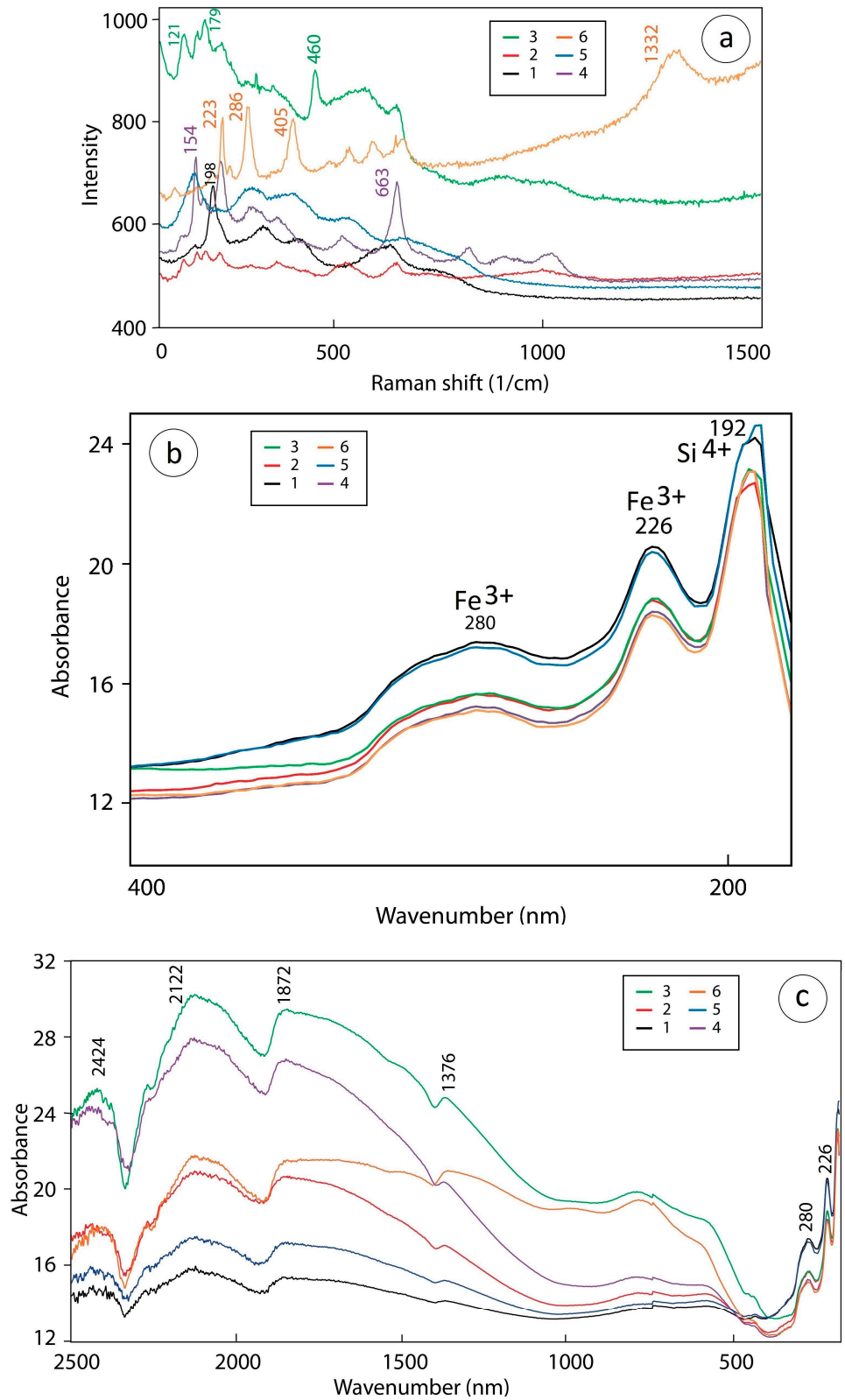

Figure 7. Raman and UV spectra of the whole-fraction heavy concentrates. (**a**) Raman spectra; (**b**) UV spectra up to 400 nm; (**c**) UV spectra up to 2500 nm. (1) Fine black sand, Wadi Thalbah, (2) Coarse black sand, Wadi Thalbah, (3) Fine wadi alluvium, Wadi Al Miyah, (4) Fine wadi alluvium, Wadi Thalbah, (5) Coarse black sand, Wadi Thalbah, and (6) Coarse wadi alluvium, Wadi Haramil.

Figure 6 provides two sets of FTIR spectra for the heavy mineral concentrates extracted from black sand on the beach and the wadi alluvium in the stream course. It is obvious that the spectra and position of bands are different in the bulk heavy concentrates (magnetic and non-magnetic) and the magnetic fraction (Figure 7a,b, respectively). In the FTIR spectra of the bulk concentrates, rich in Ca-Fe-Mg silicates as amphiboles, two bands are very characteristic: namely 459 cm^{-1} (strong) and 960 cm^{-1} (very strong). The rest (518, 647, 1470, 2850, 2918 and 3380 cm^{-1}) are weak. The lattice symmetric strong mode at the 459 cm^{-1} wavelength represents the Si-O- rocking mode or the lattice vibrational mode [67,68] whereas the very strong one at 960 cm^{-1} represents the lattice mode of the Si-O-Si vibration and the O-Si-O asymmetric stretching vibration [69]. The weak band at the wavelength 1630 cm^{-1} in the bulk concentrates is equivalent to the strong one at 1636 cm^{-1}, which indicates the dominance of magnetite in the magnetic fraction. This wavelength represents O-H bending at the surface of the oxidised magnetite. This is also confirmed by the very strong band at 3460 cm^{-1} in the magnetic fraction, which indicates a stretching vibration of H_2O due to some oxidation of magnetite by hydrolysis. However, the band at 1049 cm^{-1} in the magnetic fraction indicates the presence of Fe-oxyhydroxide or goethite as FeO(OH) [70,71]. The weak wavelength at 3380 cm^{-1} in the bulk concentrate and 3460 cm^{-1} in the magnetic fraction is possibly attributed to the stretching of the hydroxyl group of goethite and the so-called "loosely bound H_2O" on the adsorbed mineral surface [72,73].

Figure 7a shows the results of Raman shifts for the bulk heavy concentrates in six samples from the five sites. At 121 cm^{-1}, the lattice mode vibration appears [74]. The following Raman shift is localised at 198 cm^{-1}, which represents Raman-active phonons as a structural transition, particularly a Verwey transition [75]. Most likely, this indicates the Verwey transition in magnetite [76]. Sometimes, Raman spectra of magnetite-rich concentrate are characterised by this shift, which represents oxidation to ferrite during the measurement and the vibrations involving Fe^{3+} and O^{2-}, while Fe^{2+} is not directly involved [77,78]. Our Raman spectra of samples from the Saudi stream sediments have a very characteristic shift at 223 cm^{-1} representing symmetric vibration corresponding to the octahedral O-Ti-O of the Ti-bearing magnetite. On the other hand, the 460 cm^{-1} shift denoting magnetite represents an asymmetric stretching vibration of the Fe-O bond in FeO_6 octahedra [79,80]. In the case of Ti-bearing magnetite, the intensity of the bands in the Raman spectra is a sensitive indicator of Ti [81,82], and therefore they suggest the presence of titanomagnetite as confirmed by our ore microscopic and SEM-EDX analyses. Additionally, Figure 7a shows some diagnostic Raman shifts of hematite, for example at 405 cm^{-1} [83,84]. The presence of hematite in the heavy concentrates results in the hematite phonon overtone at 1332 cm^{-1} [85–87]. The Raman shift at 663 cm^{-1} indicates oxidised magnetite, possibly wüstite. According to [88], the freshness of the magnetite decreases during the measurements and magnetite experiences variable degrees of oxidation. Therefore, the formation of an oxidised Fe-bearing phase (wüstite) is expected, and consequently the Raman shift is located at 663 cm^{-1} and not at 372 cm^{-1}, which is the case for the fresh magnetite. Finally, the Raman shifts at 154 cm^{-1} and 179 cm^{-1} possibly indicate ilmenite, titanite, TiO_2 polymorphs and OH-bearing non-opaque minerals such as amphiboles [89–92].

The UV-Vis-NIR spectra of the investigated bulk heavy concentrates are shown in Figure 7b,c. A strong band at wavenumber 192 nm represents the Si^{4+} transition due to the appreciable number of silicate heavy minerals. The 226 and 280 nm wavenumbers are attributed to the intrinsic band gap absorption of the magnetite, and its oxidation products, especially when it is fine- and ultrafine-sized [93]. In other words, they represent bands of ferric iron (Fe^{3+}). Ferrous (Fe^{2+}) bands are minimal and the high wavenumber bands at 1376, 1872, 2122 and 2424 are not strong and assign divalent cations such as Ca^{2+}, Fe^{2+} and Mg^{2+} in fine-sized non-opaques, particularly amphiboles as the dominant silicate content (Figure 7c). This is more distinct in the spectra of fine heavy fractions (63–125 μm) from two stations at Wadi Al Miyah and Wadi Thalbah.

7. Conclusions

(a) In addition to Fe-Ti oxides, promising concentrates of strategic minerals in northwestern Saudi Arabia are a potential source of radionuclide minerals such as zircon/uranothorite (up to 7.2 wt% UO_2 and 17.5 wt% ThO_2). Additional resources of rare-earth elements are hosted in radioactive monazite with up to ΣREE oxides= 67.9 wt%.

(b) Whole-fraction contents of V_2O_5 (up to 0.36 wt%) and ZrO_2 (0.6 wt%) in black sand are correlated with magnetite and zircon from mafic and felsic provenances.

(c) FTIR spectra indicate lattice vibrational modes of non-opaque heavy minerals such as Fe-Ca-Mg amphibole. O-H vibrational stretching in the magnetic fraction is attributed to magnetite and Fe-oxyhydroxides such as goethite.

(d) Raman spectra indicates a Verwey transition in magnetite. The Raman shift at 223 cm^{-1} in the Ti-magnetite represents symmetric vibration of the octahedral O-Ti-O, whereas the at 460 cm^{-1} shift indicates asymmetric stretching vibration of the Fe-O bond in FeO_6 octahedra.

(e) Owing to the dominance of, Fe^{3+}, some wavenumbers (e.g., 226 and 280 nm) in the Uv-Vis-NIR spectra are distinct due to the intrinsic gap between magnetite and its oxidation products.

(f) Finally, the Si^{4+} transition at 192 nm is attributed to frequent non-opaque minerals in the heavy concentrates such as hornblende and ferrohornblende. Future X-ray photoelectron spectroscopy (XPS) analyses are recommended for the accurate evaluation of Si^{4+} and Fe cations.

Author Contributions: Conceptualization, A.A.S. and A.M.E.-T.; methodology, A.A.S. and A.M.E.-T.; software, A.A.S.; validation, A.A.S. and A.M.E.-T.; formal analysis, A.M.E.-T.; investigation, A.A.S. and A.M.E.-T.; resources, A.A.S.; data curation, A.A.S.; writing—original draft preparation, A.A.S. and A.M.E.-T.; writing—review and editing, A.A.S. and A.M.E.-T.; visualization, A.M.E.-T.; supervision, A.A.S.; project administration, A.M.E.-T.; funding acquisition, A.M.E.-T. All authors have read and agreed to the published version of the manuscript.

Funding: This research received no external funding.

Data Availability Statement: Data from our research are available upon request.

Acknowledgments: We would like to thank King Abdulaziz University (Jeddah, Saudi Arabia) for supporting the field trips and other logistics. We are especially grateful to Hesham Mokhtar (Geology Department, Cairo University) for his assistance, particularly in the spectroscopy section. Generous access to the new scanning electron microscope laboratory in the Nuclear Materials Authority (NMA) of Egypt is greatly appreciated. We thank the academic editor and two anonymous reviewers for their comments. Bobo Mao from the editorial office is highly acknowledged for her sincere helps and patience.

Conflicts of Interest: The authors declare that they have no known competing financial interests or personal relationships that could have appeared to influence the work reported in this paper.

References

1. Boyle, D.K.; Atkinson, V.G.; Sayib, K.A. *An Evaluation of Gold Placer Deposits in the Murayjib Region. Open-File-Report by Riofinex, RF-OF-04-28*; Ministry of Petroleum and Mineral Resources: Jeddah, Kingdom of Saudi Arabia, 1984.
2. Surour, A.A.; El-Kammar, A.A.; Arafa, E.H.; Korany, H.M. Dahab stream sediments, southeastern Sinai, Egypt: A potential source of gold, zircon and magnetite. *J. Geochem. Explor.* **2003**, *77*, 25–43. [CrossRef]
3. Surour, A.A.; El-Kammar, A.A.; Arafa, E.H.; Korany, H.M. Mineralogy and geochemistry of fine-grained Dahab stream sediments, Southeastern Sinai, Egypt: Emphasis on the intergrowths of Fe-Ti oxides. *Acta Geochim.* **2021**, *40*, 871–894. [CrossRef]
4. Nasir, S.; Al Sayigh, A.; Al-Safarjalani, A. Sedimentology of the lower Hofuf Formation, Eastern Province of Saudi Arabia, and the chances for gold prospection. *Neues Jahrb. Fur Geol. Und Palaontol.-Abh.* **2007**, *243*, 325–342. [CrossRef]
5. Qadhi, T.M.; Surour, A.A.; Maddah, S.S.; Basyoni, M.H. Mineralogy and economic evaluation of gold-bearing stream sediments from Wadi Al Hamd area, northwestern Saudi Arabia. *Ann. Geol. Surv. Egypt.* **2007**, *29*, 209–236.
6. Obeid, M.; Ali, M.; Mohamed, N. Geochemical exploration on the stream sediments of Gabal El Mueilha area, Central Eastern Desert, Egypt: An overview on the rare metals. *Resour. Geol.* **2008**, *51*, 217–227. [CrossRef]

7. Darwish, M.A.G.; Poellmann, H. Geochemical exploration for gold in the Nile Valley Block (A) area, Wadi Allaqi, South Egypt. *Geochemistry* **2010**, *70*, 353–362. [CrossRef]
8. El-Makky, A.M.; Sediek, K.N. Stream sediments geochemical exploration in the Northwestern part of Wadi Allaqi Area, south Eastern Desert, Egypt. *Nat. Resour. Res.* **2012**, *21*, 95–115. [CrossRef]
9. Moufti, A.M.B. Opaque mineralogy and resource potential of placer gold in the stream sediments between Duba and Al Wajh, Red Sea coast, northwestern Saudi Arabia. *J. Afr. Earth Sci.* **2014**, *99*, 188–201. [CrossRef]
10. Abdel-Karim, A.M.; Zaid, S.M.; Moustafa, M.I.; Barakat, M.G. Mineralogy, chemistry and radioactivity of the heavy minerals in the black sands, along the northern coast of Egypt. *J. Afr. Earth Sci.* **2016**, *123*, 10–20. [CrossRef]
11. Abdel-Karim, A.M.; Moustafa, M.I.; El-Afandy, A.H.; Barakat, M.G. Mineralogy, chemical chcaracteristics and upgrading of beach ilmenite of the top meter of black sand deposits of the Kafr Al-Sheikh Governorate, Northern Egypt. *Acta Geol. Sin.-Engl. Ed.* **2017**, *91*, 1326–1338. [CrossRef]
12. Darwish, M.A.G. Geochemical Stream Sediment Survey in the Wadi Umm Rilan Area, South Eastern Desert, Egypt: A new occurrence for gold mineralisation. *Acta Geol. Sin.-Engl. Ed.* **2017**, *91*, 1041–1062. [CrossRef]
13. El-Kammar, A.; El-Wakil, M.; Abd El-Rahman, Y.; Fathy, M.; Abdel-Azeem, M. Stream sediment geochemical survey of rare elements in an arid region of the Hamadat area, central Eastern Desert, Egypt. *Ore. Geol. Rev.* **2020**, *117*, 103287. [CrossRef]
14. Dawood, Y.H.; Abd El-Naby, H.H. Mineral chemistry of monazite from the black sand deposits, northern Sinai, Egypt: A provenance perspective. *Miner. Mag.* **2007**, *71*, 389–406. [CrossRef]
15. Abdel-Karim, A.M.; El-Shafey, A. Mineralogy and chemical distribution study of placer cassiterite and some associated new recorded minerals, east Rosetta, Egypt. *Arab. J. Geosci.* **2012**, *5*, 807–816. [CrossRef]
16. Young, S.M.; Pitawala, A.; Ishig, H. Geochemical characteristics of stream sediments, sediment fractions, soils, and basement rocks from the Mahaweli River and its catchment, Sri Lanka. *Chem. Erde.* **2013**, *73*, 357–371. [CrossRef]
17. Kirkwood, C.; Everett, P.; Ferreira, A.; Lister, B. Stream sediment geochemistry as a tool for enhancing geological understanding: An overview of new data from south west England. *J. Geochem. Explor.* **2016**, *163*, 28–40. [CrossRef]
18. El Aref, M.; Abd El-Rahman, Y.; Zoheir, B.; Surour, A.; Helmy, H.; Abdelnasser, A.; Ahmed, A.; Ibrahim, M. Mineral Resources in Egypt (I): Metallic Ores. In *The Geology of Egypt*; Hamimi, Z., El-Barkooky, A., Martínez Frías, J., Fritz, H., Abd El-Rahman, Y., Eds.; Springer: Cham, Switzerland, 2020; pp. 521–587.
19. Almalki, K.A.; Al Mosallam, M.S.; Aldaajani, T.; Al-Namazi, A.A. Landforms characterization of Saudi Arabia: Towards a geomorphological map. *Intern. J. Appl. Earth Observ. Geoinform.* **2022**, *112*, 102945. [CrossRef]
20. Alqahtani, F.A.; Khalil, M.K. Geochemical analysis and tectonic evaluation of the Miocene-Pliocene sequence at Al Rehaili area, Northern Jeddah, Saudi Arabia. *Arab. J. Geosci.* **2019**, *12*, 323. [CrossRef]
21. Alqahtani, F.; Khalil, M. Geochemical analysis for evaluating the paleoweathering, paleoclimate, and depositional environments of the siliciclastic Miocene-Pliocene sequence at Al-Rehaili area, Northern Jeddah, Saudi Arabia. *Arab. J. Geosci.* **2021**, *14*, 239. [CrossRef]
22. Pearse, R.W.B.; Gaydon, A.G. *The Identification of Molecular Spectra*; Chapman and Hall: London, UK; New York, NY, USA, 1976.
23. Hawthorne, F.C. Spectroscopic methods in mineralogy and geology. *Rev. Min.* **1988**, *18*, 698.
24. Rinaudo, C.; Cairo, S.; Gastaldi, D.; Gianfagna, A.; Mazziotti Tagliani, S.; Tosi, G.; Conti, C. Characterization of fluoro-edenite by μ-Raman and μ-FTIR spectroscopy. *Min. Mag.* **2006**, *70*, 291–298. [CrossRef]
25. Iezzi, G.; Della Ventura, G.; Bellatreccia, F.; Lomastro, S.; Bandli, B.R.; Gunter, M.E. Site occupancy in richterite-winchite from Libby, Montana USA, by FTIR spectroscopy. *Min. Mag.* **2007**, *71*, 93–104. [CrossRef]
26. Henderson, G.S.; Neuville, D.R.; Downs, R.T. Spectroscopic methods. *Rev. Min. Geochem.* **2014**, *78*, 800.
27. Andò, S.; Grazanti, E. Raman spectroscopy in heavy-mineral studies. In *Sediment Provenance Studies in Hydrocarbon Exploration and Production*; Scott, R.A., Smyth, H.R., Morton, A.C., Richardson, N., Eds.; Geological Society, Special Publications: London, UK, 2014; Volume 386, pp. 395–412.
28. Aceto, M.; Cala, E.; Gulino, F.; Gullo, F.; Labate, M.; Agostino, A.; Picollo, M. The use of UV-Visible diffuse reflectance spectrophotometry for a fast, preliminary authentication of gemstones. *Molecules* **2022**, *27*, 4716. [CrossRef]
29. Nehlig, P.; Genna, A.; Asfirane, A.; Guerrot, C.; Eberlé, J.M.; Kluyver, H.M.; Lasserre, J.L.; Le Goff, E.; Nicol, N.; Salpeteur, N.; et al. A review of the Pan-African evolution of the Arabian Shield. *GeoArabia* **2002**, *27*, 103–124. [CrossRef]
30. Johnson, P.R. Explanatory notes to the map of Proterozoic geology of Western Saudi Arabia. Technical Report SGS-TR-2006-4. 2006, 62p. Available online: https://faculty.ksu.edu.sa/sites/default/files/Explanatory%20notes%20for%20the%20shield%20SGS-TR-2006-4.pdf (accessed on 30 May 2024).
31. Moufti, A.M.B. Mineralogy and mineral chemistry of auriferous stream sediments from Al Wajh area, NW Saudi Arabia. *Arab. J. Geosci.* **2009**, *2*, 1–17. [CrossRef]
32. Davies, F.B. *Explanatory Notes on the Geologic Map of Al Wajh Quadrangle, Sheet 26 B*; Ministry of Petroleum and Mineral Resources, Deputy Ministry for Mineral Resources: Jeddah, Kingdom of Saudi Arabia, 1985; 27p.
33. Grammatikopoulos, T.; Mcken, A.; Hamilton, C.; Christiansen, O. A vanadium-bearing magnetite and ilmenite mineralization and beneficiation from the Sinarsuk V-Ti project, West Greenland. *Cim. Bull.* **2002**, *95*, 87–95.
34. Wu, B.; Cao, J.; Tang, Y.; Zou, J.; Yu, Z. Geological features of the vandium-titanium-magnetite deposit in the Hongge area and its geophysical prospecting. *Geol. Explor.* **2012**, *48*, 140–147.

35. Abdel-Karim, A.M.; Barakat, M.G. Separation, upgrading, and mineralogy of placer magnetite in the black sands, northern coast of Egypt. *Arab. J. Geosci.* **2017**, *10*, 298. [CrossRef]
36. Lee, S. A review on types of vanadium deposits and process mineralogical characteristics. *J. Korean Soc. Min. Energy Resour. Engin.* **2020**, *57*, 640–651. [CrossRef]
37. Khedr, M.Z.; Zaghloul, H.; Takazawa, E.; El-Nahas, H.; Azer, M.K.; El-Shafei, S.A. Genesis and evaluation of heavy minerals in black sands: A case study from the southern Eastern Desert of Egypt. *Geochemistry* **2023**, *83*, 125945. [CrossRef]
38. Habtoor, A.; Ahmed, A.H.; Harbi, H. Petrogenesis of the Alaskan-type mafic-ultramafic complex in the Makkah quadrangle, western Arabian Shield, Saudi Arabia. *Lithos* **2016**, *263*, 33–51. [CrossRef]
39. Surour, A.A.; Ahmed, A.H.; Harbi, H.M. Mineral chemistry as a tool for understanding the petrogenesis of Cryogenian (arc-related) Ediacaran (post-collisional) gabbros in the western Arabian Shield of Saudi Arabia. *Int. J. Earth Sci. (Geol. Rundsch)* **2017**, *106*, 1597–1617. [CrossRef]
40. Gahlan, H.A.; Azer, M.K.; Al-Hashim, M.H.; Osman, M.S.M. New insights and constraints on the Late Neoproterozoic post-collisional mafic magmatism in the Arabian Shield, Saudi Arabia. *Lithos* **2023**, *436*, 106989. [CrossRef]
41. Abdel-Karim, A.M. Petrographic and chemical characterization of Fe-Ti oxides and sulfides hosted in mafic intrusions, south Sinai, Egypt: Implication for genesis. *J. Geol. Min. Res.* **2009**, *1*, 067–093.
42. Khedr, M.Z.; Takazawa, E.; Arai, S.; Stern, R.J.; Morishita, T.; El-Awady, A. Styles of Fe-Ti-V ore deposits in the Neoproterozoic layered mafic-ultramafic intrusions, south Eastern Desert of Egypt: Evidence for fractional crystallization of V-rich melts. *J. Afr. Earth Sci.* **2022**, *194*, 104620. [CrossRef]
43. Najorka, J.N.; Gottschalk, M.; Franz, G.; Heinrich, W. Ca-Sr distribution among amphibole, clinopyroxene, and chloride-bearing solutions. *Am. Mineral.* **1999**, *84*, 596–606. [CrossRef]
44. Eldougdoug, A.; Abd El-Rahman, Y.; Harbi, H. The Ediacaran post-collisional Khamal gabbro-anorthosite complex from the Arabian Shield and its Fe-Ti-P ore: An analogy to Proterozoic massif-type anorthosites. *Lithos* **2020**, *372*, 105674. [CrossRef]
45. Broska, I.; Harlov, D.; Tropper, P.; Siman, P. Formation of magmatic titanite and titanite–ilmenite phase relations during granite alteration in the Tribeč Mountains, Western Carpathians, Slovakia. *Lithos* **2007**, *95*, 58–71. [CrossRef]
46. Angiboust, S.; Harlov, D. Ilmenite breakdown and rutile-titanite stability in metagranitoids: Natural observations and experimental results. *Am. Mineral.* **2017**, *102*, 1696–1708. [CrossRef]
47. Moustafa, M.I. Mineralogy and Beneficiation of Some Economic Minerals in the Egyptian Black Sands. Ph.D. Thesis, Mansoura University, Mansoura, Egypt, 1999.
48. Al Safarjalani, A.M. *Placer Gold Deposits in the Hofuf Formation, the Eastern Province of Saudi Arabia*; Research Project No. 4022; King Faisal University: Riyadh, Kingdom of Saudi Arabia, 2004; 99p.
49. Moufti, A.M.B.; Qadhi, T.M. Abnormal concentrations of boron, gold and heavy metals in the Pleistocene and Recent terraces at Wadi Al Hamd, northwestern KSA. *J. King Abdulaziz Univ. Earth Sci. Sect.* **2009**, *20*, 67–91. [CrossRef]
50. Abd El-Naby, H.H.; Dawood, Y.H. Testing the validity of detrital zircon chemistry as a provenance indicator. *Arab. J. Geosci.* **2014**, *7*, 341–353. [CrossRef]
51. Hoskin, P.W.O.; Kinny, P.D.; Wyborn, D.; Chappell, B.W. Identifying accessory mineral saturation during differentiation in granitoid magmas: An integrated approach. *J. Petrol.* **2000**, *41*, 1365–1396. [CrossRef]
52. Belousova, E.A.; Griffin, W.L.; O'Reilly, S.Y.; Fisher, N.I. Igneous zircon: Trace element composition as an indicator of source rock type. *Contrib. Miner. Petrol.* **2002**, *143*, 602–622. [CrossRef]
53. Darby, D.A.; Tsang, Y.W. Variation in ilmenite element composition within and among drainage basins: Implications for provenance. *J. Sed. Petrol.* **1987**, *57*, 831–838.
54. Ramdohr, P. *The Ore Minerals and Their Intergrowths*; Pergamon Press: Oxford, UK, 1980; 1207p.
55. Rao, D.S.; Murthy, G.V.S.; Rao, K.V.; Das, D.; Chintalapudi, S.N. Alteration characteristics of beach placer ilmenite from Chatrapur coast, Orissa, India. *J. Appl. Geochem.* **2002**, *4*, 47–59.
56. Pownceby, M.I. Alteration and associated impurity element enrichment in detrital ilmenites from the Murray Basin, southeast Australia: A product of multistage alteration. *Austr. J. Earth Sci.* **2010**, *57*, 243–258. [CrossRef]
57. Haggerty, S.E. Opaque mineral oxides in terrestrial igneous rocks. In *Oxide Minerals*; Rumble, D., Ed.; Walter de Gruyter GmbH: Berlin, Germany, 1976; pp. 101–300.
58. Reynolds, I.M. The iron-titanium oxide mineralogy of Karoo dolerite in the eastern Cape and southern Orange Free State. *Trans. Geol. Soc. South Africa* **1983**, *86*, 211–220.
59. Geissman, J.W.; Strangway, D.W.; Tasillo-Hirt, A.M.; Jensen, I.S. Paleomaenetism of Late Archean metavolcanics and metasediments Abitibi orogen, Canada: Tholeiites of the Kinojevrs Group. *Can. Earth Sci.* **1983**, *20*, 436–461. [CrossRef]
60. Cassidy, K.F.; Groves, D.I.; Binns, R.A. Manganoan ilmenite formed during regional metamorphism of Archean mafic and ultramagic rocks from Western Australia. *Can. Mineral.* **1988**, *26*, 999–1012.
61. Surour, A.A.; Moufti, A.M.B. Opaque mineralogy as a tracer the magmatic history of volcanic rocks: An example from the Neogene-Quaternary Harrat Rahat intercontinental volcanic field, north western Saudi Arabia. *Acta Geol. Sin.-Engl. Ed.* **2013**, *87*, 1281–1305. [CrossRef]
62. Ross, S.D. *Inorganic Infrared and Raman Spectra*; McGraw-Hill Book Company Ltd.: London, UK, 1972; 414p.
63. Bouchard, M.; Smith, D.C. Catalogue of 45 reference Raman spectra of minerals concerning research in art history or archaeology, especially on corroded metals and coloured glass. *Spectrochim Acta Part A* **2003**, *59*, 2247–2266. [CrossRef]

64. Petriglieri, J.R.; Bersani, D.; Andò, S.; Lottici, P.P. Identification of impurities in gemological materials by means of photoluminescence using micro-Raman apparatus. In Proceedings of the GeoRaman Xth Meeting, Nancy, France, 11–13 June 2012. Extend Abstract.
65. Durie, R.A.; Rosevear, P. *A Study of the Potential of Infrared Spectroscopy for the Rapid Identification and Estimation of Minerals in Beach Sands and Their Concentrate*; Investigation Report No. 85; Commonwealth Scientific and Industrial Research Organization, Division of Mineral Chemistry: Sydney, NSW, Australia, 1970; 28p.
66. Bower, D.; Misra, P.; Peterson, M.; Howard, M.; Hewagama, T.; Gorius, N.; Li, S.; Asalam, S.; Livengood, T.; McAdam, K.J. Comparative VIS and NIR Raman and FTIR spectroscopy of lunar analog samples. In Proceedings of the Europlanet Science Conference, Madrid, Spain, 23–28 September 2012. EPSC Volume 14, Extended Abstract No 427.
67. Andrut, M.; Gottschalk, M.; Melzer, S.; Najorka, J. Lattice vibrational modes in synthetic tremolite-Sr-tremolite and tremolite-richterite solid solutions. *Phys. Chem. Miner.* **2000**, *27*, 301–309. [CrossRef]
68. Reig, F.B.; Adelantado, J.V.G.; Moya Moreno, M.C.M. FTIR quantitative analysis of calcium carbonate (calcite) and silica (quartz) mixtures using the constant ratio method: Application to geological samples. *Talanta* **2002**, *58*, 811–821. [CrossRef] [PubMed]
69. Della Ventura, G.; Vigliaturo, R.; Gieré, R.; Pollastri, S.; Gualtieri, A.F.; Iezzi, G. FTIR spectroscopy of the regulated asbestos amphiboles. *Minerals* **2018**, *8*, 413. [CrossRef] [PubMed]
70. Betancur, A.F.; Pérez, F.R.; Correa, M.M.; Barrero, C.A. Quantitative aproach in iron oxides and oxihydroxides by vibrational analysis. *Opt. Pura Y Apl.* **2012**, *45*, 269–275. [CrossRef]
71. Veneranda, M.; Aramendia, J.; Bellot-Gurlet, L.; Colomban, P.; Castro, K.; Madariaga, J.M. FTIR spectroscopic semi-quantification of iron phases: A new method to evaluate the protection ability index (PAI) of archaeological artefacts corrosion systems. *Corros. Sci.* **2018**, *133*, 68–77. [CrossRef]
72. Ruran, H.D.; Frost, R.L.; Kloprogge, J.T. The behavior of hydroxyl units of synthetic goethite and its dehydroxylated product hematite. *Spectrochim Acta Part A Mol. Biomol. Spectrosc.* **2001**, *57*, 2575–2586. [CrossRef]
73. Omran, M.; Fabritius, T.; Elmahdy, A.M.; Abdel-Khalek, N.A.; El-Aref, M.; Elmanawi, A. XPS and FTIR spectroscopic study on microwave treated high phosphorus iron ore. *Appl. Surf. Sci.* **2015**, *345*, 127–140. [CrossRef]
74. Bertie, J.E. Lattice modes of molecular crystals. In *Analytical Applications of FT-IR to Molecular and Biological Systems*; Durig, J.R., Ed.; NATO Advanced Study Institutes Series Springer: Dordrecht, Netherlands, 1980; Volume 57, pp. 433–465.
75. Degiorgi, L.; Blatter-Merke, I.; Wachter, P. Magnetite: Phonon modes and the Verwey transition. *Phys. Rev. B-Conden Matter Mater Phys.* **1987**, *35*, 5421. [CrossRef]
76. Gasparov, L.V.; Tanner, D.B.; Romero, D.B.; Berger, H.; Margaritondo, G.; Forro, L. Infrared and Raman studies of the Verwey transition in magnetite. *Phys Rev B-Conden. Matter Mater Phys.* **2000**, *62*, 7939–7944. [CrossRef]
77. Shebanova, O.L.; Lazor, P. Raman spectroscopic study of magnetite ($FeFe_2O_4$): A new assignment for the vibrational spectrum. *J. Solid State Chem.* **2003**, *174*, 424–430. [CrossRef]
78. Shebanova, O.L.; Lazor, P. Raman study of magnetite (Fe_3O_4): Laser-induced thermal effects and oxidation. *J. Raman Spectrosc.* **2003**, *34*, 845–852. [CrossRef]
79. Graves, P.R.; Johnston, C.; Campaniello, J.J. Raman scattering in spinel structure ferrites. *Mater Res. Bull.* **1988**, *23*, 1651–1660. [CrossRef]
80. Baddour-Hadjean, R.; Pereira-Ramos, J.-P. Raman microspectrometry applied to the study of electrode materials for lithium batteries. *Chem. Rev.* **2010**, *110*, 1278–1319. [CrossRef]
81. Wang, A.; Kuebler, K.E.; Jolliff, B.L.; Haskin, L.A. Raman spectroscopy of Fe-Ti-Cr-oxides, case study: Martian meteorite EETA79001. *Am. Mineral.* **2004**, *89*, 665–680. [CrossRef]
82. Zinin, P.; Tatsumi-Petrochilos, L.; Bonal, L.; Acosta, T.; Hammer, J.; Gilder, S.; Fuller, M. Raman spectroscopy of titanomagnetites: Calibration of the intensity of Raman peaks as a sensitive indicator for their Ti content. *Am. Mineral.* **2011**, *96*, 1537–1547. [CrossRef]
83. Beattie, I.R.; Gilson, T.R. The single-crystal Raman spectra of nearly opaque materials. Iron(III) oxide and chromium(III) oxide. *J. Chem. Soc. A Inorg. Phys. Chem.* **1970**, *5*, 980–986. [CrossRef]
84. Chamritski, I.; Burns, G. Infrared- and Raman-active phonons of magnetite, maghemite, and hematite: A computer simulation and spectroscopic study. *J. Phys. Chem. B* **2005**, *109*, 4965–4968. [CrossRef]
85. McCarty, K.F. Inelastic light scattering in α-Fe_2O_3: Phonon vs. magnon scattering. *Solid State Commun.* **1988**, *68*, 799–802. [CrossRef]
86. Massey, M.J.; Baier, U.; Weber, W.H. Effects of pressure and isotopic substitution on the Raman spectrum of α-Fe_2O_3: Identification of two-magnon scattering. *Phys. Rev. B-Conden Matter Mater Phys.* **1990**, *41*, 7822–7827. [CrossRef] [PubMed]
87. Shim, S.-H.; Duffy, T.S. Raman spectroscopy of Fe_2O_3 to 62 GP. *Am. Mineral.* **2002**, *87*, 318–326. [CrossRef]
88. Muralha, V.S.F.; Rehen, T.; Clark, R.J.H. Characterisation of iron smelting slag from Zimbabwe by Raman spectroscopy and electron beam analysis. *J. Raman Spectrosc.* **2011**, *42*, 2077–2084. [CrossRef]
89. De Faria, D.L.A.; Silva, S.V.; de Oliveira, M.T. Raman microspectroscopy of some iron oxides and oxyhydroxides. *J. Raman Spectrosc.* **1997**, *28*, 873–878. [CrossRef]
90. Sbroscia, M.; Della Ventura, G.; Iezzi, G.; Sodo, A. Quantifying the A-site occupancy in amphiboles: A Raman study in the OH-stretching region. *Eur. J. Mineral.* **2018**, *30*, 429–436. [CrossRef]

91. Maftei, A.E.; Buzatu, A.; Damian, G.; Buzgar, N.; Dill, H.; Apopei, A.L. Micro-Raman—A tool for the heavy mineral analysis of gold placer-type deposits (Pianu Valley, Romania). *Minerals* **2020**, *10*, 988. [CrossRef]
92. Stanish, E.A.; Turenne, N.N.; Connell, S.A.; Cloutis, E.A.; Applin, D.M. Single grain spectroscopic analysis of olivine, pyroxene and ilmenite. In Proceedings of the 51st Annual Lunar and Planetary Science Conference, Woodlands, TX, USA, 16–20 March 2020. Extended Abstract #2261.
93. Takai, Z.I.; Mostafa, M.K.; Asman, S.; Sekak, K.A. Preparation and characterization of magnetite (Fe_3O_4) nanoparticles by Sol-Gel method. *Intern. J. Nanoelectron Mater* **2019**, *12*, 37–46.